Metrologia

Ytterbium optical lattice clock with instability of order 10^{-18}

OPEN ACCESS
IOP Publishing | Bureau International des Poids et Mesures Metrologia

Metrologia **59** (2022) 065009 (9pp) https://doi.org/10.1088/1681-7575/ac99e4

Ytterbium optical lattice clock with instability of order 10^{-18}

Ang Zhang[1,3], Zhuanxian Xiong[1], Xiaotong Chen[2], Yanyi Jiang[2,*], Jinqi Wang[1,3], Congcong Tian[1,3], Qiang Zhu[1], Bing Wang[1], Dezhi Xiong[1], Lingxiang He[1], Longsheng Ma[2] and Baolong Lyu[1,*]

[1] Key Laboratory of Atomic Frequency Standards, Innovation Academy for Precision Measurement Science and Technology, Chinese Academy of Sciences, Wuhan 430071, People's Republic of China
[2] State Key Laboratory of Precision Spectroscopy, East China Normal University, Shanghai 200062, People's Republic of China
[3] University of Chinese Academy of Sciences, Beijing 100049, People's Republic of China

E-mail: yyjiang@phy.ecnu.edu.cn and baolonglyu@apm.ac.cn

Received 29 April 2022, revised 12 October 2022
Accepted for publication 13 October 2022
Published 2 November 2022

Abstract

We have built an ytterbium optical lattice clock with improvements over our previous version. An in-vacuum blackbody radiation (BBR) shield is employed to provide a well characterized BBR environment. The effective temperature felt by the atoms can be determined at an accuracy level of 13 mK, leading to a total BBR frequency shift uncertainty of 9.5×10^{-19}. We have also built an ultra-stable optical cavity system to pre-stabilize the clock laser, achieving a flicker frequency instability of $\sim 3 \times 10^{-16}$. Rabi spectroscopy of the lattice-trapped atoms can achieve sub-Hertz linewidth spectra. Two ytterbium clocks have been operated in an antisynchronized configuration, with real-time BBR-Stark-shift corrections applied to both of them. By comparing the two clocks, we demonstrate a single-clock instability of 5.4×10^{-18} in 4500 s. This clock will be applied for frequency comparisons to other optical clocks of different atomic species in the future.

Keywords: optical lattice clock, ytterbium atoms, Rabi spectroscopy, frequency instability

(Some figures may appear in colour only in the online journal)

1. Introduction

The past two decades have witnessed tremendous progress in optical clocks based on single-ions or lattice trapped neutral atoms. Both the frequency uncertainty and stability of the state-of-the-art optical clocks have reached the 10^{-18} level and beyond [1–9]. Best fractional frequency stabilities ever achieved were demonstrated in Sr and Yb lattice clocks [3, 4]. These two types of clocks have reached a maturity such that they now can be incorporated into the existing time scales [10–16]. Transportable lattice clocks have been used for relativistic geodesy [17–19], and may also be applied for space missions aboard space stations or in deep space [20–22]. With increasing precision, optical clocks will find their applications in more areas.

We here report the development and operation of an ytterbium (^{171}Yb) lattice clock. As we have known, the frequency uncertainty and long-term stability of an optical lattice clock depend mainly on how well the systematic frequency shifts can be controlled, while the short-term stability is mainly limited by the clock laser. Compared with our previous version [23, 24], the new clock has an in-vacuum blackbody radiation (BBR) shield, providing a more uniform thermal radiation environment. Additionally, the frequency noise of the clock laser is further reduced by being pre-stabilized to an ultrastable optical cavity with increased cavity length. Further more, the

* Authors to whom any correspondence should be addressed.

orientation of the optical lattice is changed from horizontal to vertical. The tight confinement in the vertical direction allows a lower light intensity to support the atoms against gravity, enabling a larger lattice beam size which leads to a lower atomic density, and hence a reduced collision frequency shift. We have realized closed-loop operation of this clock using Rabi spectroscopy. Comparison of two ytterbium lattice clocks shows a single-clock instability of 5.4×10^{-18} after 4500 s of averaging.

2. Clock setup

Our optical clock setup is actually an improved version of the previous setup that has been described in detail elsewhere [23, 24]. The major changes in the design are as follows: (I) the science chamber body is made from titanium instead of stainless steel, in order to further reduce the residual magnetization. (II) The Zeeman slower is removed, which avoids the heating effect and the stray magnetic field from the magnetic field coils. We use a 399 nm red-detuned light to decelerate the atoms from the atomic oven. (III) A vertically aligned optical lattice is adopted. Compared with a horizontal optical lattice, a vertical lattice not only suppresses the atomic tunneling between adjacent lattice sites [25], but also allows a lower light intensity to support the atoms against gravity owing to the tight vertical confinement. We can thus use a larger beam size to reduce the atomic density, and hence the collision frequency shift. (IV) A BBR shield is placed inside the science chamber to enclose the cold atoms, creating an environment of high-thermal-uniformity. (V) An ultra-stable optical cavity affording improved frequency stability is used for pre-stabilizing the clock laser.

2.1. BBR shield

As shown in figure 1, our in-vacuum BBR shield is very similar as that first developed at NIST [26]. The internal surfaces of the copper body are coated with nano graphite powder blended with ultra-high vacuum epoxy. This easily obtainable coating material has both high emissivity and good electrical conductivity. Besides, a typical transparent conductive coating of indium tin oxide (ITO) has been applied to all the inside surfaces of the BK7 glass windows. A pair of holes with a diameter of 6 mm allows the 759 nm optical lattice beam to pass through the shield without any loss.

Four platinum resistance temperature detectors (RTDs) distributed throughout the copper body provide a real-time measurement of the shield's temperature. We embedded these RTDs (Sensing Devices; PT100/8AX*) in the copper shield by inserting them into holes with a diameter of 1.7 mm and a depth of 6 mm. To improve the thermal contact, all the RTDs had been covered with silicone resin before fixed in the holes. One additional RTD is fixed on the internal surface of the vacuum flange in figure 1 to measure the temperature of vacuum chamber. NIST traceable calibration of these RTDs have been provided by the manufacturer. In our experiment the resistances of the RTDs are measured by a digital multimeter

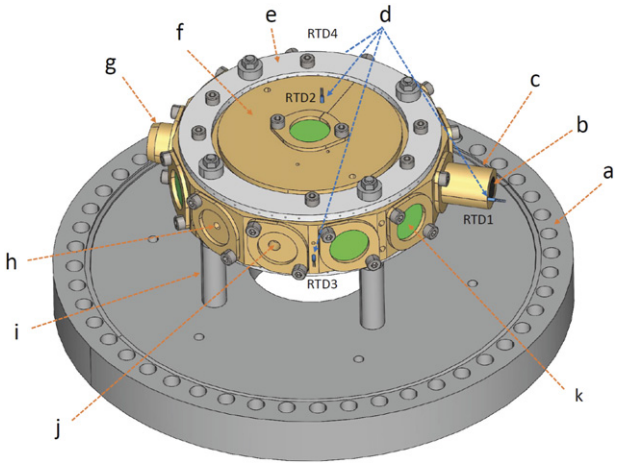

Figure 1. Solidworks rendering of the in-vacuum BBR shield. Notable features include: (a) titanium flange; (b) nano-graphite powder coating; (c) atomic beam exit aperture; (d) four RTDs embedded in the shield (RTD4 is on the back side of the shield, facing RTD3); (e) boron nitride rings used for heating the shield; (f) copper construction; (g) atomic beam entry aperture; (h) one of the two holes for 399 nm probe beam; (i) steatite support tube (×4); (j) one of the two holes for both the 759 nm lattice beam and the 578 nm clock laser beam; (k) BK7 glass windows with ITO conductive coating (×8). For scale, the flange is 10 inch in diameter.

(34420A, Keysight) which has been referenced to an ultra-stable standard reference resistor (Tinsley 5685) to realize real-time calibration.

Data acquisitions of the RTDs and the reference resistor are arranged in successive clock cycles. The sense current is a short pulse of 160 ms applied during the interrogation time of the clock. Each sensor (including the reference resistor) is sensed every 20 clock cycles. The temperature value of each sensor is given by the average of six measurements, and thus updated with a period of 120 clock cycles. We use a low RTD sense current of 100 μA to reduce the self-heating effect. We have measured the self heating of each RTD, and found that RTD2 has the maximum self heating. With a constant sense current of 1 mA, the temperature of RTD2 increases with a time constant of about 7.5 s. When the steady state is reached, the temperature has been elevated by 0.77 K. For the pulsed sense current actually used in the clock, the self-heating effect is about 0.2 mK. We use a value of 1 mK as the conservative estimate of the uncertainty for self-heating.

In figure 2(a), we see that the science chamber temperature has a slow change up to about 1 K in 4 h, whereas the average temperature of the BBR shield shows a slower change. On the other hand, the temperature gradient across the BBR shield is directly displayed by the reading of the four RTDs on the copper body. The temperature deviations of these RTDs from their average temperature are rather small, well below 10 mK (see figure 2(b)). Note that, the accuracy of the measured temperature is limited by the combined uncertainty of the manufacturer calibration and the digital multimeter, which is comparable to the observed temperature differences. Therefore, the real temperature inhomogeneity is possibly much smaller than the difference between the temperature reading.

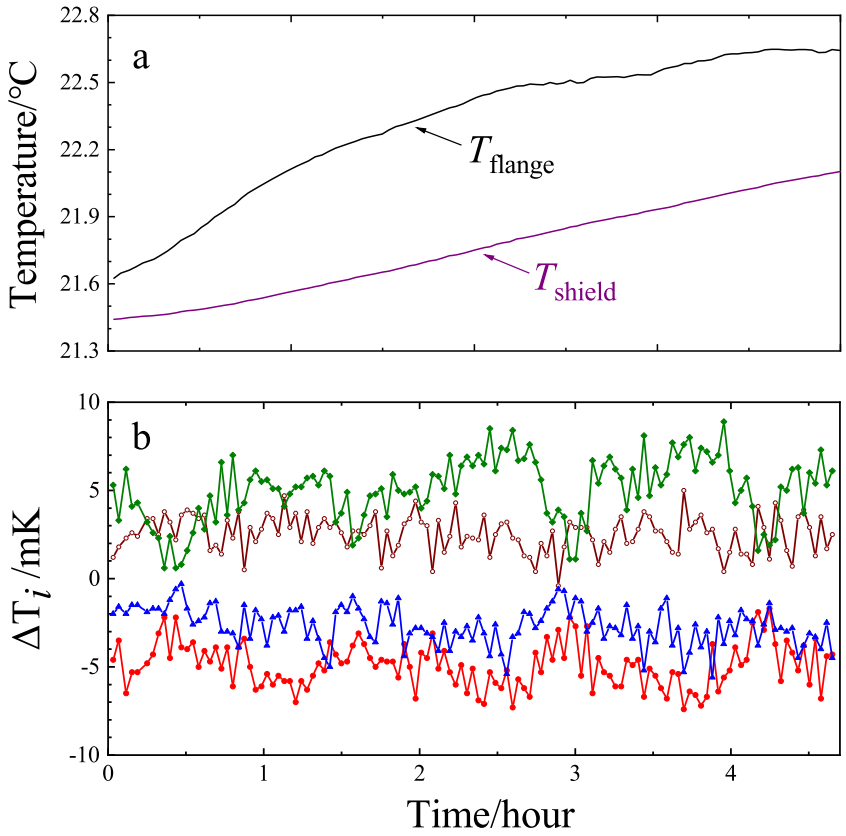

Figure 2. Temperature measurement of the BBR shield. Temperatures of the four RTDs embedded in the shield, as well as the one on the flange, were repeatedly sampled every 2 min, and recorded for a total time of 4 h while the clock is in normal operation state. (a) $T_{\rm shield}$ is the average temperature of the four RTDs on the shield. (b) ΔT_i represents the temperature deviation of the ith RTD from $T_{\rm shield}$.

The very low temperature inhomogeneity should be accounted for by both the copper body's excellent heat conductivity and the thermal insulation provided by the vacuum environment.

Since the BBR shield forms a nearly full enclosure to the lattice-trapped atoms, the effective temperature $T_{\rm eff}$ felt by the atoms depends mainly upon the thermal radiation from the BBR shield, which can be well characterized by the average temperature of the shield body. However, the outside thermal radiation is not totally shielded. Firstly, there are apertures for the atomic beam or light beams. Secondly, the optical windows have a weak transmission for the BBR radiation. The outside radiation sources generally have a different temperature compared to the BBR shield, thus leading to slight shifts in $T_{\rm eff}$. For quantitative description, we first calculate the effective solid angles for each radiation source. This is performed by using the finite element analysis to the thermal radiation of the BBR shield, the same method as used in our previous work [27]. Then, for each radiation source, the shift in $T_{\rm eff}$ is estimated according to the corresponding effective solid angle and temperature difference.

The effective solid angles of the optical windows and apertures depend upon the inner coating emissivity, ε, of the copper body. The higher the emissivity, the smaller the effective solid angles. For example, the effective solid angle of the entry aperture, $\Omega^{\rm eff}_{\rm entry}$, can reduced by a factor of ~ 2 when ε is increased from 0.2 to 0.8. If the effective solid angle of a component in the BBR shield becomes smaller, the effective temperature $T_{\rm eff}$ is less strongly affected by the thermal radiations coming through this component. Note also that effective solid angles are not linear functions of the emissivity. Instead, they become more and more insensitive to the emissivity variation as ε increases. Taking again the entry aperture as an example, we find that $\Omega^{\rm eff}_{\rm entry}$ is only reduced by about 2% when ε is increased from 0.8 to 0.85. Clearly, a high emissivity provides another advantage that the accuracy of an effective solid angle is only slightly affected by the emissivity uncertainty.

In the calculation of effective solid angles, we adopted an emissivity value of $\varepsilon = 0.8$ for the inner coating, which is a typical value for graphite powder. The effective solid angle of the entry aperture is $\Omega^{\rm eff}_{\rm entry}/4\pi = 0.0015$. The corresponding external environment may have a temperature different from $T_{\rm eff}$. However, the temperature difference is well below 5 K. So, we can safely set an uncertainty of 7.5 mK for the entry aperture. Our 6 mm-thick BK7 glass windows have a very small residual transmission ($t_{\rm win} < 0.001$) to room-temperature BBR, and their total effective solid angle is $\Omega^{\rm eff}_{\rm win} = 4\pi \times 0.236$. As viewed by the atoms, the residual thermal radiation imbalance causes a small change of $T_{\rm eff}$ which can be written as [27]

$$\delta T^{\rm win}_{\rm eff} = (T_{\rm vac} - T_{\rm eff})\frac{\Omega^{\rm eff}_{\rm win}}{4\pi} t_{\rm win},$$

where $T_{\rm vac}$ is the temperature of the vacuum chamber surrounding the BBR shield. For a temperature difference as large

Table 1. Effective temperature uncertainty budget for our ^{171}Yb lattice clock at ∼295 K.

Effects	Uncertainty/mK
RTDs temperature measurements	
Manufacturer calibration	5
Digital multimeter (4-wire)	5
Self heating	1
Temperature inhomogeneity and effective solid angles	
Entry aperture	7.5
Exit aperture	2.0
Probe aperture	0.6
Lattice beam aperture	1.2
Atomic oven	4.7
BK7 windows	0.5
Copper shield	5.8
Total	13

as 2 K between $T_{\rm vac}$ and $T_{\rm eff}$, $\delta T_{\rm eff}^{\rm win}$ is below 0.47 mK. We thus set an effective temperature uncertainty of 0.5 mK for windows.

The atomic oven subtends a very small effective solid angle of $\Omega_{\rm oven}^{\rm eff}/4\pi = 8.3 \times 10^{-6}$. In operation state, the oven works at a high temperature of $T_{\rm oven} = 673$ K. Its thermal radiation would shift $T_{\rm eff}$ up by a small quantity $\Delta T_{\rm eff}^{\rm oven}$, which can be expressed as

$$\left(T_{\rm eff} + \Delta T_{\rm eff}^{\rm oven}\right)^4 = \frac{\Omega_{\rm oven}^{\rm eff}}{4\pi} T_{\rm oven}^4 + \left(1 - \frac{\Omega_{\rm oven}^{\rm eff}}{4\pi}\right) T_{\rm eff}^4.$$

Then, $\Delta T_{\rm eff}^{\rm oven}$ is determined to be 15 mK. Even if $T_{\rm oven}$ is assumed to have an uncertainty as large as 50 K, the uncertainty of $\Delta T_{\rm eff}^{\rm oven}$ is only 4.7 mK.

We have summarized in table 1 the uncertainties associated with the BBR environment, including also the temperature non-uniformity of the BBR shield. It means that the average temperature of the BBR shield, with a correction $\Delta T_{\rm eff}^{\rm oven}$, can represent the effective temperature within the specified uncertainty range. The total uncertainty of 13 mK corresponds to a BBR Stark shift of 4.3×10^{-19} for the clock transition of ^{171}Yb. Apart from the BBR environment, the uncertainty of atomic response, arising mainly from dynamic correction η_1, also leads to an uncertainty on the BBR Stark shift, which is about 8.5×10^{-19} at the room temperature [26]. The total BBR Stark shift is thus 9.5×10^{-19} for our clock. As shown in figure 2(a), the BBR shield temperature is changing slowly due to the heating of the magnetic coils for magneto-optical trap. In the operation of the clock, the slow drift of the BBR Stark shift must be compensated. To this end we have applied real-time frequency corrections to the interrogation light through an acousto-optic modulator (AOM). In the same work mentioned above [26], the dependence of BBR Stark shift upon the absolute temperature $T_{\rm eff}$ has been experimentally confirmed in a range from the room temperature to about 360 K. So, we just use the formula therein and the measured $T_{\rm eff}$ to calculate the BBR Stark shift.

It should be noted that the BBR shield also acts as a Faraday shield. The copper body together with the conductive coatings on the optical windows form a Faraday shield which will prevent the enclosed atoms from dc Stark shifts. In fact, a more sophisticated Faraday shield developed at NIST had been demonstrated to have the dc Stark shift suppressed to a level below 10^{-20} [28].

2.2. Optical cavity

The 578 nm clock laser light is generated from a 1156 nm laser (Toptica; TA Pro) by frequency-doubling in a periodically poled lithium niobate (PPLN) waveguide. We lock the clock laser to a 30 cm-long ULE optical cavity (cavity-1 in figure 3). The finesse of the Fabry–Pérot cavity is determined to be about 2.1×10^5 by cavity ring-down measurement. Compared to the 10 cm-long cavity used in our previous works, the longer reference cavity has a reduced thermal noise limit, estimated to be $\sim 2 \times 10^{-16}$. To ensure the stability of the reference frequency, the cavity needs a well controlled environment that should provide vacuum environment, thermal insulation, temperature stabilization, acoustic isolation and active vibration isolation. Additionally, the optics needed for mode matching of the light must be mounted near the cavity. The design and performance evaluation has been described in detail elsewhere [29]. The whole reference cavity setup was built by our team members at East China Normal University, Shanghai, and then transported to Wuhan where the main clock setup stays. Before transportation, the cavity was taken out from the vacuum chamber for the sake of safety. After arriving at Wuhan, it was put back, and the vacuum chamber was then repumped.

We measure the clock laser coherence using the same method described in reference [30]. As shown in figure 3(a), while the clock laser is locked to cavity-1, the output light at the fundamental wavelength is frequency shifted and locked to another cavity with the aid of a frequency shifter (AOM2). The second cavity (cavity-2) is a commercial one, with the same cavity length, but designed for the fundamental wavelength.

Besides the same cavity length, the two cavities have spacers of the same shape, and mirror substrates of the same type. So, their thermal noise limits are close to each other. Since the two cavity setups sit on the ground of the same room, with a distance less than 4 m, the seismic noise sources felt by them are very similar. Active vibration isolation platforms with the same model number have been equipped in the two setups. In addition, electronic circuit modules with the same model number are employed for frequency locking. We thus know that technical frequency noises of the two cavity setups, associated with the vibration and servo loops, have approximately the same level.

The frequency difference between the two isolated and independent cavities can be extracted from the correction frequency applied to AOM2. The fractional frequency instability of a single cavity is thus obtained, under the assumption that the two cavities have identical noise levels but are uncorrelated (see figure 3(b)). For the averaging time of 1–100 s, the frequency instability is roughly flat, showing a noise floor of $\sim 3 \times 10^{-16}$. Despite the similarities on thermal noise limit

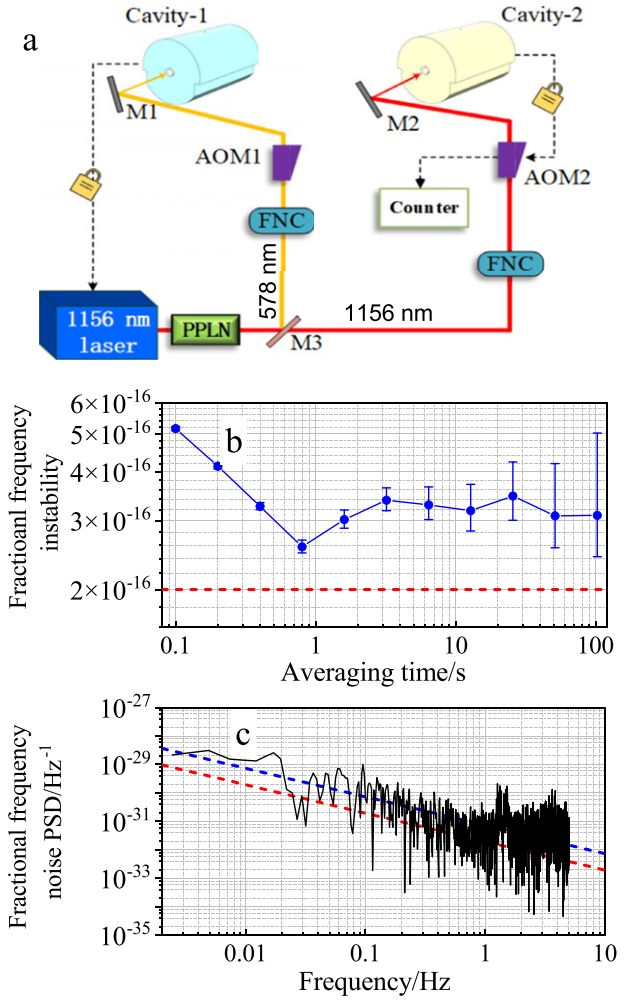

Figure 3. (a) Setup for measuring cavity noise. The clock laser is locked to cavity-1 using Pound–Drever–Hall detection. The light at the fundamental wavelength after the PPLN waveguide is frequency shifted and locked to cavity-2 through an acousto-optic-modulator (AOM2). The correction frequency applied to AOM2 provides the difference between the two cavities, and is counted to determine the frequency stability. FNC, fiber noise canceler. (b) Fractional frequency instability of one cavity. Blue circles are derived from frequency counting with a CNT-91 counter (a gate time of 100 ms, with linear drift removed). The Allan deviation has been divided by $\sqrt{2}$ to reflect the performance of a single cavity. (c) Fractional frequency noise power spectral density (S_y) of one cavity (black line). The blue dashed line is a fit curve with flicker frequency noise shape, showing a noise level of $7.3 \times 10^{-32}/f$. The red dashed lines in both (b) and (c) represent the predicted thermal noise floor of cavity-1.

and technical noise source, the two cavities are not identical. It is more reasonable to assign all technical noise contribution to one cavity, setting a lower bound and an upper bound for the frequency instability. The frequency stability of each cavity can thus be accessed to be in the range of $(2.0–3.7) \times 10^{-16}$. In the Dick noise calculation later in section 4, we use a frequency noise spectrum obtained under the assumption that both cavities contribute the same amount of frequency noise to the beat signal. The calculated Dick-noise-limited frequency instability agrees well with the observed combined Allan deviation. This agreement indicates that the two cavities most likely have approximately equal frequency instabilities. By checking the fractional frequency noise power spectral density in figure 3(c), we see that the clock laser exhibits a flicker frequency noise spectrum indeed. To deal with the frequency drift of our clock laser, we add a linear drift compensation in the following experiment by applying a correction frequency to the relevant AOM.

The frequency instability of our clock laser is $\sim 50\%$ higher than that reported in reference [29], despite that the same cavity setup has been used. The degradation in performance of our clock laser is possibly due to the following facts: first, different types of clock lasers are adopted in the two works. In reference [29], the clock laser is derived from frequency summing of a fiber laser and a Nd:YAG laser. In contrast, our clock laser is derived from the frequency doubling of a diode laser with a tapered amplified. Different frequency noise properties of the free-running clock lasers may make the achievable instability level to be laser dependent although the same cavity is used for frequency stabilizing. Second, the laboratory environments are also different. The residual seismic vibration noise felt by the cavity in Wuhan is generally not the same as that in Shanghai.

3. Spectroscopy and frequency comparison

Preparation of cold atoms starts with the conventional two-stage laser cooling, followed by loading of a 759 nm optical lattice formed by retroreflecting a focused light beam with a beam waist of 56 μm. About 2000 atoms are trapped in the lattice. Then, quenched sideband cooling is applied to the lattice-trapped Yb atoms, as first demonstrated in a clock comparison work [31]. It requires a clock laser light tuned to the red sideband of the $^1S_0$–$^3P_0$ clock transition and a 1388 nm quenching light. The entire cooling sequence consists of interleaved 578 nm cooling pulses and 1388 nm quenching pulses, lasting for 60 ms. Effectiveness of the sideband cooling is evidenced by the sideband spectra in figure 4(a). The longitudinal trap frequency and trap depth are determined to be 60 kHz and 25 μK, respectively. Owing to sideband cooling, the longitudinal temperature is reduced to $\sim$1 μK, corresponding to an average motional quantum number of $\langle n \rangle \simeq 0.1$. Now that nearly all of them have populated in a single motional state, the atoms will feel a more uniform Rabi frequency in the later interrogation stage. Next, the atoms are optically pumped to either one of the ground-state spin projections ($m_F = \pm 1/2$).

After state preparation, Rabi interrogation is performed by applying a π pulse of 578 nm probe light to excite the π transitions between the two clock states. Stepping the probe light frequency across the clock transition gives a Rabi spectrum. Two typical spectroscopic line shapes have been displayed in figure 4. For interrogation times less than 1 s, the linewidths of the observed spectral lines are Fourier-limited. With longer interrogation time, we indeed observed narrower spectrum, but the linewidth is a bit above the Fourier limit. The smallest linewidth we have achieved is 0.47 Hz at an interrogation time of 2 s. In normal clock operation, the clock laser is frequency-stabilized to a Rabi spectrum for a given interrogation time. A stable and well-resolved Rabi spectrum is required to ensure

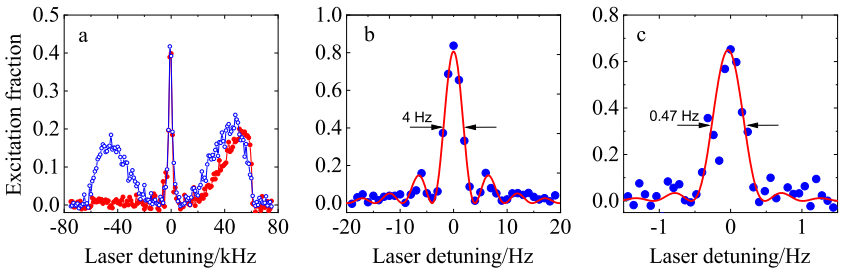

Figure 4. Rabi spectroscopy of lattice-trapped ^{171}Yb atoms. (a) Motional sideband spectra of the lattice-trapped atoms with (red circles) and without (blue open circles) sideband cooling. They are obtained by scanning the clock transition with a Rabi pulse time of 50 ms and a Rabi frequency on the order of 1 kHz. The longitude temperature is reduced from 8 μK to ∼1 μK. The trap frequency is determined to be 60 kHz from the sharp edge of the blue sideband, corresponding to a trap depth of 25 μK. (b) and (c) Single-scan Rabi spectra with an interrogation time of 200 ms and 2 s, respectively. Each red line is a fit to the Rabi lineshape.

that the servo locking is easy and robust. So we adopted a moderate linewidth of 4 Hz (interrogation time of 200 ms) which is about eight times wider than the narrowest achievable linewidth.

We found that clock Yb-2 is insensitive to the electromagnetic interference of the subway line which is about 300 m away from our laboratory. Both the spectroscopy of clock transition and the servo loop are nearly unaffected when the subway is running. In contrast, clock Yb-1 can only work at night to avoid the subway operation time. Otherwise, the error signal is very noisy as subway trains pass by, leading to intermittent unlocks. We have measured the magnetic field of the subway line using a magnetometer. The magnetic field of the subway line, $\mathbf{B}_{\rm sub}$, is a slowly varying signal with frequency components below 1 Hz. It has an amplitude of ∼10 mG, and its vector is along the vertical direction. In our old version clock Yb-1, a bias magnetic field $\mathbf{B}_0$ is applied along the vertical direction to define the quantization direction and split the two π transitions. Since the two magnetic fields add directly in magnitude, $\mathbf{B}_{\rm sub}$ causes a clock frequency fluctuation of ±2 Hz. In clock Yb-2, a bias field of 2 G is applied along the horizontal direction instead. In this case, $\mathbf{B}_0$ and $\mathbf{B}_{\rm sub}$ add in quadrature. Compared to Yb-1, the magnitude fluctuation of the total magnetic field is reduced by a factor of $2B_0/B_{\rm sub}$. Consequently, the clock frequency fluctuation of Yb-2 is reduced to the order of millihertz, and no noticeable disturbance appears in the Rabi spectrum.

To assess the frequency instability, we have carried out a frequency comparison between this clock and the old one. Both clocks, referred to as Yb-1 and Yb-2, stay in the same room, but their atomics units sit on two different experimental tables. They share the same clock laser stabilized on cavity-1, as shown in figure 5(A). Different from the newly built Yb-2, Yb-1 has a horizontal optical lattice formed by a more tightly focused 759 nm laser beam (beam waist of 45 μm). Based on the similar atomic preparation sequence as for Yb-2, it can now create a cold atom sample of ∼ 3000 atoms in the lattice. The atom number is significantly lower than before, because the viewport facing the atomic oven has been coated by ytterbium. The temperature distribution of its science chamber is monitored by 13 RTDs attached on the external surfaces. The effective temperature to the atoms can be determined with an accuracy of 160 mK [27]. The BBR Stark shift is compensated by applying a frequency correction every 120 clock cycles to the interrogation light, just as for Yb-2. Since the control of systematic shifts is not as good as that of Yb-2, the Rabi spectrum linewidth of Yb-1 only reaches ∼1 Hz. For a robust locking, we use an interrogation time of 100 ms (linewidth of 8 Hz), two times shorter than that of Yb-2.

Optical lattice lights are derived from a Ti:sapphire laser (M squared, SolsTiS). This laser is stabilized to a ULE cavity, and the frequency drift is measured to be ∼ 8 kHz per day. In clock operation, the laser is tuned to the magic frequency $\nu_{\rm zero}$ determined in reference [32]. Without a second 759 nm laser, we have to allow this laser to be shared by the two clocks. After years of aging, this laser at present is unable to provide enough power for simultaneous lattice trapping in different clocks. To circumvent the problem, the laser light is periodically switched between the two clocks. This means that the atomic systems can only be interrogated antisynchronously, rather than synchronously. The time sequence in figure 5(B) shows the timing for atom preparation, interrogation, and state readout.

The frequency correction signals $f_{1,2}(t)$ is displayed in figure 5(C) for a three-hour interval. The mean frequency difference between $f_2(t)$ and $f_1(t)$, which is about 0.4 Hz, has been deducted in figure 5(C). This nonzero mean value is mainly caused by the different collision shifts of the two atomic samples. The Allan deviation of the fluctuating frequency difference represents the combined frequency instability of the two clocks, which has reached 7.6×10^{-18} at the averaging time of 4500 s. Assuming that both clocks have equal frequency instability, and all noise processes are uncorrelated between the two systems, the single clock instability is just given by dividing the combined instability by $\sqrt{2}$. As shown in figure 5(D), the single clock instability reaches 5.4×10^{-18} at 4500 s. Since the clock servo loops are set to deal only with slow frequency fluctuations, they have an attack time of a few 10 s, evidenced by the instability bump near 20 s. If the Allan deviations are fitted to a shape corresponding to the white frequency noise type, we will get an asymptote of $4.6 \times 10^{-16}/\sqrt{\tau}$ (the red line in figure 5(D)).

The fact that two clocks share the same lattice laser may lead to common-mode rejection to some kinds of lattice-induced frequency shifts. In a reported work on Yb lattice clock [32], the lattice-induced frequency shift has been measured precisely near the magic frequency $\nu_{\rm zero}$, and confirmed

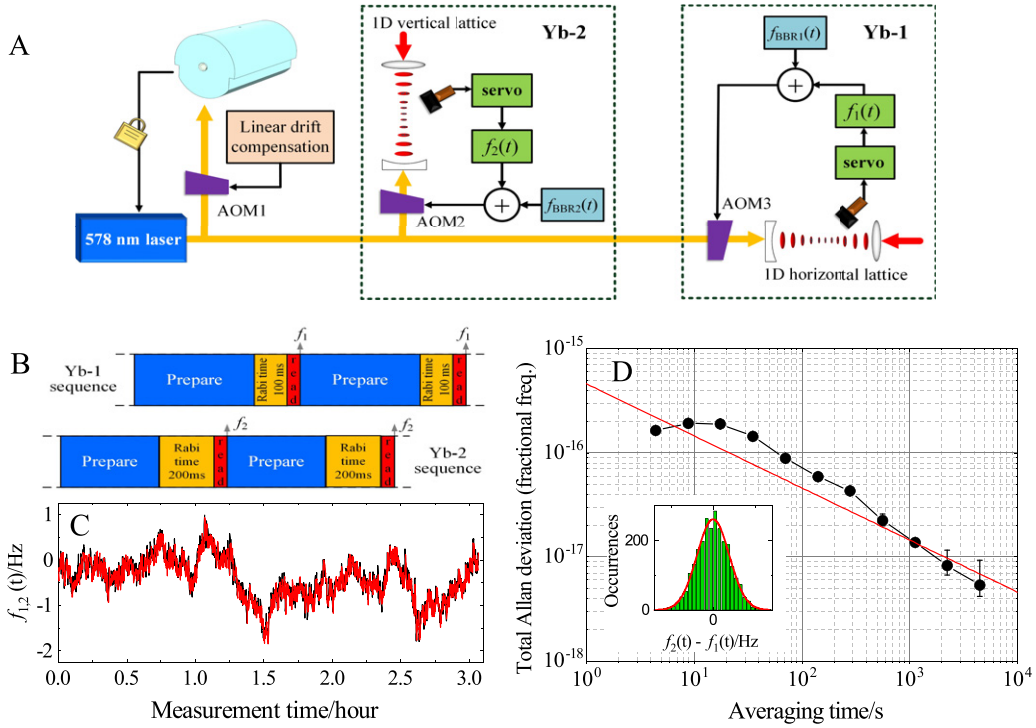

Figure 5. Frequency comparison between the Yb optical lattice clocks. (A) Experimental scheme. $f_{1,2}(t)$ are correction frequencies from the servo loops, whereas $f_{\mathrm{BBR1}}(t)$ and $f_{\mathrm{BBR2}}(t)$ correspond to the BBR Stark frequency shifts of Yb-1 and Yb-2, respectively. (B) Time sequence for antisynchronous interrogation of the two clocks (the time axis is not to scale). (C) Correction frequencies, $f_{1,2}(t)$, are shown in red and black. The mean frequency difference of 0.4 Hz has been removed. (D) The frequency instability of a single clock, represented by the Allan deviation of $[f_2(t) - f_1(t)]/\sqrt{2}$ (black circles). Error bars indicate 1σ confidence intervals. The red line represents the white-frequency-noise fit of $4.6 \times 10^{-16}/\sqrt{\tau}$. The inset is a histogram of all data of and a Gaussian fit ($\chi^2_{\mathrm{r}} = 0.9895$).

to be an inverted parabolic function of the trap depth. Using the parameters therein, we can estimate the clock frequency drift due to the lattice light. The frequency drift of our lattice laser is less than 8 kHz, and the resulted fractional frequency drift is below 10^{-19}. On the other hand, the light power stability also affect the frequency instability. The output power of the 759 nm laser is constant at a level better than 1%. Assuming that the frequency offset of the lattice light from ν_{zero} is as high as 10 MHz, the long-term frequency instability due to the slow light power fluctuation is about 6×10^{-19}. Even if these slow frequency drifts are not common-mode rejected, they are small enough to be neglected for instabilities in the order of 10^{-18}.

4. Analysis of Dick noise

It is well known that periodic interrogation in a clock will cause the so-called Dick noise which is actually the down conversion of the local oscillator frequency noise. For a single optical clock, the Dick noise limited Allan variance is given by [33]

$$\sigma_y^2(\tau) = \frac{1}{\tau}\sum_{m=1}^{\infty}\frac{|g_m|^2}{g_0^2}S_y\left(\frac{m}{T_{\mathrm{c}}}\right), \qquad (1)$$

where T_{c} is the clock cycle time, and $S_y(f)$ is the one-sided power spectral density of the relative frequency fluctuation of the clock laser. The mean value and the mth Fourier component of the sensitivity function $g(t)$ are defined as follows:

$$g_0 = \frac{1}{T_{\mathrm{c}}}\int_0^{T_{\mathrm{c}}} g(t)\mathrm{d}t,$$

$$g_m = \frac{1}{T_{\mathrm{c}}}\int_0^{T_{\mathrm{c}}} g(t)\mathrm{e}^{\mathrm{i}2\pi mt/T_{\mathrm{c}}}\,\mathrm{d}t.$$

Note that, for both clocks, the interrogation times are significantly shorter than the cycle length of $T_{\mathrm{c}} = 1.1$ s. Based on the already measured frequency noise level of the clock laser, as well as the time sequences for clock cycles, we have used equation (1) to calculate the two clocks' Allan variances, yielding $4.3 \times 10^{-16}/\sqrt{\tau}$ for Yb-1, and $3.7 \times 10^{-16}/\sqrt{\tau}$ for Yb-2.

In the situation that two clocks not only share the same clock laser, but also have the same T_{c}, Dick noise between the two systems is correlated. In analogy to equation (1), the Dick noise level in the frequency difference of the two clock can be expressed by the following variance:

$$\sigma_{y12}^2(\tau) = \frac{1}{\tau}\sum_{m=1}^{\infty}\left|\frac{g_{1m}}{g_{01}} - \frac{g_{2m}}{g_{02}}\right|^2 S_y\left(\frac{m}{T_{\mathrm{c}}}\right)$$

$$= \frac{1}{\tau}\sum_{m=1}^{\infty}\left|\frac{g_{1m}}{g_{01}} - \frac{g_{2m}^{\mathrm{syn}}}{g_{02}}\mathrm{e}^{\mathrm{i}2\pi m\Delta t/T_{\mathrm{c}}}\right|^2 S_y\left(\frac{m}{T_{\mathrm{c}}}\right), \qquad (2)$$

where g_{0i} and g_{im} $(i = 1, 2)$ are the mean value and the mth Fourier component of the sensitivity function for the ith clock, respectively. The time delay Δt between the interrogation pulse of Yb-1 and that of Yb-2 represents the general case that

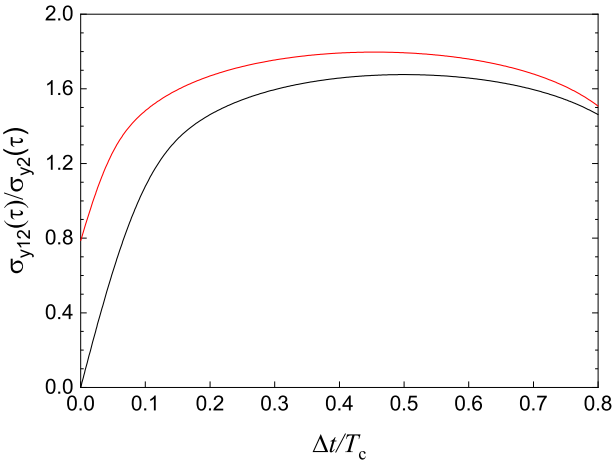

Figure 6. Calculated Dick noise level in frequency comparison, normalized by the Dick noise level $\sigma_{y2}(\tau)$ of the singe clock Yb-2. The synchronized and antisynchronized configurations correspond to $\Delta t/T_c = 0, 0.5$, respectively. $S_y(f)$ has been assumed to scale as $1/f$. For the red curve, parameters are the same as the experimental ones except the variable $\Delta t/T_c$ ($T_c = 1.1$ s; Rabi interrogation times are 100 ms and 200 ms for Yb-1 and Yb-2, respectively.) The black curve is the result under the same conditions except that Yb-1 has been assumed to have the same interrogation time as Yb-2.

two clocks are not in synchronization. $g_{2m}^{\rm syn}$ denotes the value of g_{2m} in the special case that Yb-2 is synchronized with Yb-1. The right side of equation (2) includes the down-conversion of the clock laser noise at all the harmonic frequencies of $1/T_c$. Obviously, for Dick noise components of different order number m, the relative phases between the two systems are generally different.

We have calculated $\sigma_{y12}(\tau)$ as a function of $\Delta t/T_c$, using the experimental parameters for our clocks. In the antisynchronized configuration ($\Delta t/T_c = 0.5$), the result is $\sigma_{y12}(\tau) = 6.58 \times 10^{-16}/\sqrt{\tau}$. This deviation, if divided by the factor $\sqrt{2}$, gives a frequency instability level of $4.65 \times 10^{-16}/\sqrt{\tau}$, which agrees well with the fitting curve of the measured single-clock instability in figure 5. It indicates that the Dick noise almost totally dominates the frequency instability. The ratio of $\sigma_{y12}(\tau)$ to the Dick noise $\sigma_{y2}(\tau)$ of the single clock Yb-2 has also been calculated for varied $\Delta t/T_c$. As shown by the red curve in figure 6, Dick noise between the two clocks can only be partly canceled even in the synchronized configuration due to the fact that $g_{1m}/g_{01} \neq g_{2m}/g_{02}$. In the antisynchronized configuration, σ_{y12}/σ_{y2} reaches the maximum value of 1.79, noticeably larger than $\sqrt{2}$. If we use this ratio value to interpret the measured combined Allan deviation, the frequency instability of Yb-2 would become lower than we claimed in section 3, reaching 4.2×10^{-18} at 4500 s. Anyway, in order to avoid underestimating the frequency noise level of Yb-2, we prefer to claim the more conservative instability level that was obtained using the ratio value of $\sqrt{2}$. The black curve in figure 6 represents a situation where both clock have the same interrogation time of 200 ms. Now, Dick noise can be completely canceled in the synchronized configuration. In contrast, σ_{y12}/σ_{y2} has a maximum value of 1.68 in the antisynchronized configuration.

5. Discussion and summary

Yb-2 clock can be further improved by employing cavity-enhanced optical lattice. The two optical windows on the science chamber, which allow the lattice light to pass through, are AR-coated at two wavelengths of 759 nm and 578 nm. According to the measured insertion loss, an optical cavity with mirrors outside the science chamber is able to enhance the light power by a factor of 30. The beam size can be set a few times larger. This way, the atomic density, and hence the collision shifts, can be substantially reduced. Alternatively, we can keep the beam size unchanged, but let the light intensity be enhanced. Then, the lattice-induced frequency shift can be measured with larger lever arms. We also plan to add a new 759 nm laser in the future. With each clock having an independent lattice laser, they can be compared in a synchronous configuration, enabling a common-mode rejection of the Dick noise. This way, the frequency instability will average down much faster.

In summary, we have demonstrated an ytterbium lattice clock with improved performance provided mainly by an in-vacuum BBR shield and an ultra-stable ULE cavity of low thermal noise limit. The BBR shield has provided a uniform thermal radiation environment, and the BBR Stark shift uncertainty can thus be determined at a level of 10^{-18}. The fabricated ULE cavity has been used to stabilize the frequency of our clock laser, reducing the short-term instability to $\sim 3 \times 10^{-16}$. In Rabi spectroscopy of the clock transition, sub-hertz linewidths have been achieved. We have also performed frequency comparison between two clocks, and found that the frequency instability of each clock is Dick noise limited, and averages down to 5.4×10^{-18} after 4500 s. We expect to realize frequency comparisons between this Yb clock and other single-ion clocks in our institute in the near future.

Acknowledgments

This work is supported by the Natural Science Foundation of China (Grants No. U20A2075, and No. 11803072), by the National Key Research and Development Program of China (Grants No. 2017YFA0304402, and No. 2017YFA0304403), by the Strategic Priority Research Program of the Chinese Academy of Sciences under Grant No. XDB21030100, and by the Project supported by the Space Application System of China Manned Space Program.

ORCID iDs

Zhuanxian Xiong https://orcid.org/0000-0002-2015-3878

References

[1] Bothwell T, Kedar D, Oelker E, Robinson J, Bromley S, Tew W, Ye J and Kennedy C 2019 *Metrologia* **56** 065004
[2] Brewer S M, Chen J S, Hankin A M, Clements E R, Chou C W, Wineland D J, Hume D B and Leibrandt D R 2019 *Phys. Rev. Lett.* **123** 033201

[3] Oelker E *et al* 2019 *Nat. Photon.* **13** 714–9
[4] McGrew W F *et al* 2018 *Nature* **564** 87–90
[5] Schioppo M *et al* 2017 *Nat. Photon.* **11** 48–52
[6] Huntemann N, Sanner C, Lipphardt B, Tamm C and Peik E 2016 *Phys. Rev. Lett.* **116** 063001
[7] Ushijima I, Takamoto M, Das M, Ohkubo T and Katori H 2015 *Nat. Photon.* **9** 185–9
[8] Yao Y, Li B, Yang G, Chen X, Hao Y, Yu H, Jiang Y and Ma L 2021 *Photon. Res.* **9** 98–105
[9] Huang Y *et al* 2022 *Phys. Rev. Appl.* **17** 034041
[10] Kobayashi T, Akamatsu D, Hosaka K, Hisai Y, Wada M, Inaba H, Suzuyama T, Hong F L and Yasuda M 2020 *Metrologia* **57** 065021
[11] Ido T, Hachisu H, Nakagawa F and Hanado Y 2016 *J. Phys.: Conf. Ser.* **723** 012041
[12] Grebing C *et al* 2016 *Optica* **3** 563–9
[13] Lodewyck J *et al* 2016 *Metrologia* **53** 1123–30
[14] Hachisu H, Nakagawa F, Hanado Y and Ido T 2018 *Sci. Rep.* **8** 4243
[15] Yao J, Parker T E, Ashby N and Levine J 2018 *IEEE Trans. Ultrason. Ferroelectr. Freq. Control* **65** 127–34
[16] Yao J *et al* 2018 *Navigation* **65** 601–8
[17] Takano T *et al* 2016 *Nat. Photon.* **10** 662–6
[18] Grotti J *et al* 2018 *Nat. Phys.* **14** 437–41
[19] Takamoto M, Ushijima I, Ohmae N, Yahagi T, Kokado K, Shinkai H and Katori H 2020 *Nat. Photon.* **14** 411–5
[20] Bongs K *et al* 2015 *C. R. Phys.* **16** 553–64
[21] Guo F *et al* 2021 *AIP Adv.* **11** 125116
[22] Kolkowitz S, Pikovski I, Langellier N, Lukin M D, Walsworth R L and Ye J 2016 *Phys. Rev.* D **94** 124043
[23] Zhang M J, Liu H, Zhang X, Jiang K L, Xiong Z X, Lü B L and He L X 2016 *Chin. Phys. Lett.* **33** 070601
[24] Liu H, Zhang X, Jiang K L, Wang J Q, Zhu Q, Xiong Z X, He L X and Lyu B L 2017 *Chin. Phys. Lett.* **34** 020601
[25] Lemonde P and Wolf P 2005 *Phys. Rev.* A **72** 033409
[26] Beloy K *et al* 2014 *Phys. Rev. Lett.* **113** 260801
[27] Xiong D Z, Zhu Q, Wang J Q, Zhang A, Tian C C, Wang B, He L X, Xiong Z X and Lyu B L 2021 *Metrologia* **58** 035005
[28] Beloy K *et al* 2018 *Phys. Rev. Lett.* **120** 183201
[29] Jin L, Jiang Y, Yao Y, Yu H, Bi Z and Ma L 2018 *Opt. Express* **26** 18699–707
[30] Jiang Y Y, Ludlow A D, Lemke N D, Fox R W, Sherman J A, Ma L S and Oates C W 2011 *Nat. Photon.* **5** 158–61
[31] Nemitz N, Ohkubo T, Takamoto M, Ushijima I, Das M, Ohmae N and Katori H 2016 *Nat. Photon.* **10** 258–61
[32] Brown R C *et al* 2017 *Phys. Rev. Lett.* **119** 253001
[33] Audoin C, Santarelli G, Makdissi A and Clairon A 1998 *IEEE Trans. Ultrason. Ferroelectr. Freq. Control* **45** 877–86